WILEY-VCH

FULL PAPER

High Performance Magnetically Separable G-C_3N_4/γ-Fe_2O_3/TiO_2 Nanocomposite with Boosted Photocatalytic Capability towards the Cefixime Trihydrate Degradation under Visible-Light

Roya Jahanshahi,[a] Sara Sobhani*[a] and José Miguel Sansano[b]

[a] Department of Chemistry, College of Sciences, University of Birjand, Birjand, Iran.
E-mail: ssobhani@birjand.ac.ir, sobhanisara@yahoo.com
[b] Departamento de Química Orgánica, Facultad de Ciencias, Centro de Innovación en Química Avanzada (ORFEO-CINQA) and Instituto de Síntesis Orgánica (ISO), Universidad de Alicante, Apdo. 99, 03080-Alicante, Spain.

Supporting information for this article is given *via* a link at the end of the document.

Abstract: A magnetically separable g-C_3N_4/γ-Fe_2O_3/TiO_2 nanocomposite is synthesized as an intensely effectual visible-light-driven photocatalyst. It is fully characterized by FT-IR, XPS, XRD, VSM, DRS, SEM, TEM, BET, EDS, and elemental mapping techniques. Based on the Tauc plot of $(\alpha h\nu)^2$ *vs.* hυ, the value of band gap energy for g-C_3N_4/γ-Fe_2O_3/TiO_2 is estimated to be 2.6 eV, which proves the high capability of the catalyst to enhance the photoinduced electron-holes separation and improves its visible-light photocatalytic performance. The high photocatalytic activity of this catalyst towards the cefixime trihydrate (CEF) degradation, under visible-light radiationcan, be ascribed to the synergistic optical effects between g-C_3N_4, γ-Fe_2O_3, and TiO_2. Using central composite design (CCD) based on response surface methodology (RSM), the maximum degradation efficiency of about 98% was obtained at the optimal conditions comprising the CEF amount of 20 mg/L, photocatalyst value of 0.04 g/L, irradiation intensity of 9 W/m^2, and pH of 5.5, at 90 min. Utilizing an innocuous visible-light source, almost complete mineralization of CEF (based on TOC analysis), using a very low amount of photocatalyst, applying air as the oxidant, and convenient magnetic separation of the catalyst from the reaction media and its ease of recycling for at least seven consecutive runs are the major highlights of this protocol.

Introduction

Nowadays, a growing general concern has emerged regarding the subject of environmental contaminations by releasing the residues of pharmaceutical ingredients in the aqueous media.[1] Antibiotics considered as growing pollutants that required a particular consideration owing to their continuous consumption in medical, veterinary and aquaculture.[2] Most of these extensively used chemotherapeutic agents are resistant against the biodegradation, so their elimination through the conventional wastewater treatment plans would be challenging. For this reason, their residual even at very low concentrations is a serious risk for human health and aquatic organisms in the coming years.[3] Therefore, the development of effectual techniques for the mineralization of these pollutants has become a mandatory issue.[4,5]

Various physical and chemical methodologies have been reported for the elimination of antibiotics from wastewater, comprising the ion exchange processes,[6] reverse osmosis,[7] coagulation-flotation,[8] adsorption,[9] membrane filtration,[10] different advanced oxidation processes (AOPs),[5] etc. Due to the capability of complete degradation of contaminants compared with the most mentioned techniques, AOPs appears to be more promising alternatives.[11,12] In the 1970s, heterogeneous photocatalysis was emerged as one of the novel AOPs and received an increasing growth with every passing year.[13] In this context, semiconductor-based heterogeneous photocatalysis is known as the most superior technique for the green and facile elimination of antibiotics from wastewater.[14,15] Recently, graphitic carbon nitride (g-C_3N_4), a polymeric metal-free material has been extensively investigated as a semiconductor photocatalyst.[16] Although it has the benefits of easy manufacture, excellent visible-light harvesting ability (band gap = 2.73 eV), nontoxicity, low-cost and high thermal/chemical stability, the low separation efficiency and fast recombination rate of the photo-generated electrons and holes significantly confine its photocatalytic performance.[17-21] One of the most efficient proposed approaches to amend the visible-light photocatalytic properties of g-C_3N_4 is its combination with other semiconductors to prepare composite photocatalysts.[22-27] TiO_2 is one of the most favorable semiconductor candidates in the photocatalytic degradation area due to its outstanding features including chemical and physical durability, photo-corrosion resistance, low toxicity, and cost-effectiveness.[28-30] However, the main challenging aspect of using TiO_2 is its broad band gap (Eg = 3.2 eV) that limits its photocatalytic performance only to the UV-light area (3-5% of the total solar energy).[31] Furthermore, the photo-generated electron-hole pairs in TiO_2 can readily recombine, which critically diminish its optical efficiency.[32] Fascinatingly, the semiconductor combination of g-C_3N_4 with TiO_2 can overcome the elevated recombination speed of the resultant photo-excited electron and hole pairs of both semiconductors.[33] It also enhances the visible-light absorption potential of TiO_2.[34]

Cefixime trihydrate (CEF), which belongs to the cephalosporin drugs category, is a type of β-lactam antibiotics. The low bioavailability of this antibiotic has limited its adsorption by the gastrointestinal tract,[35] leads to serious environmental damages. CEF is effective while encountering various kinds of pathogenic bacteria.[36] This antibiotic is not only operative in treating an extensive range of bacterial infectious diseases but also can be utilized to prevent infection in the people undergoing severe surgical operations.[37] To the best of our knowledge, the photocatalytic degradation of CEF is limited to a few methods using NiO/nano-clinoptilolite,[36] nano α-Fe_2O_3/ZnO,[38] TiO_2/nitrogen doped holey graphene hybrid[3] and nano-crystalline ZnO.[39] These procedures suffer from one or more of the following difficulties such as using large amounts of photocatalyst, loss of the photocatalyst during recycling, long periods, low amounts of the degradation efficiency, and most importantly the employment of detrimental light sources and complex photoreactors. Thus, the

necessity of promoting more proficient and durable photocatalytic systems for CEF degradation is evident.

Considering the importance of using green and safe light sources and convenient catalyst recovery and recycling in wastewater treatment processes, and in continuation of our persistent research interest in introducing new magnetically recyclable heterogeneous nanocatalysts[40-46] herein, we have reported the fabrication of a high-performance g-C_3N_4/γ-Fe_2O_3/TiO_2 nanocomposite. After its characterization by various techniques, it was utilized as a magnetically separable visible-light-driven photocatalyst towards the CEF degradation under the blue LED illumination. Moreover, the central composite design (CCD) along with response surface methodology (RSM) was carried out for modeling and optimizing the photocatalytic degradation protocol.

Results and Discussion

Synthesis and characterization of g-C_3N_4/γ-Fe_2O_3/TiO_2 nanocomposite

According to the multi-step procedure presented in scheme 1, g-C_3N_4/γ-Fe_2O_3/TiO_2 magnetic nanocomposite was prepared by a sol-gel procedure from tetra-*n*-butyl orthotitanate (TBOT) in the presence of a mixture of separately synthesized g-C_3N_4 and γ-Fe_2O_3 (*see the supporting information for details*). Then, the photocatalytic system was well characterized *via* a collection of various techniques.

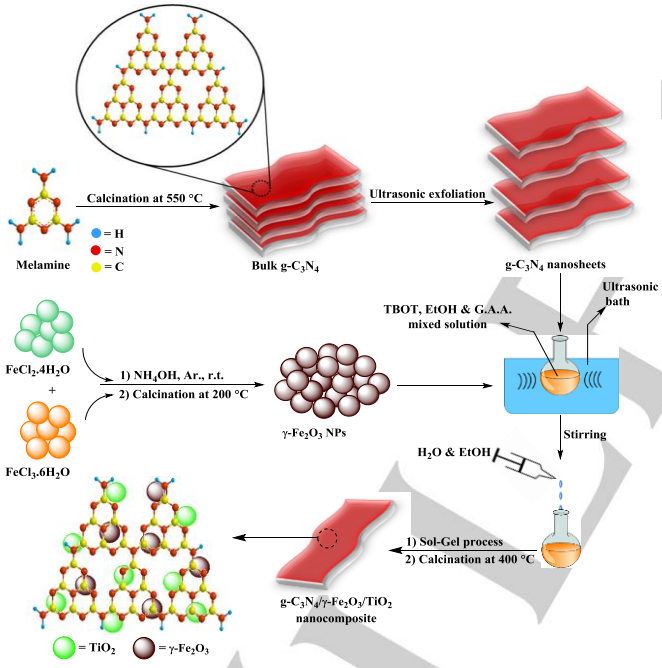

Scheme 1. Overall flowchart for the fabrication of g-C_3N_4/γ-Fe_2O_3/TiO_2.

FT-IR spectra of g-C_3N_4, γ-Fe_2O_3 and g-C_3N_4/γ-Fe_2O_3/TiO_2 are shown in Figure 1. In the FT-IR spectrum of g-C_3N_4 (Figure 1a), the intense adsorption band at around 808 cm^{-1} is ascribed to the breathing mode of triazine units.[47] The strong adsorption bands at about 1238–1641 cm^{-1} could be attributed to the stretching vibration frequencies of both aromatic C–N and C=N bonds.[48] Besides, the observed broad band at around 3000–3450 cm^{-1} could be attributed to the stretching vibration frequencies of the NH and NH_2 groups.[2] The FT-IR spectrum of γ-Fe_2O_3 (Figure 1b) exhibited a wide absorption band at about 542–695 cm^{-1}, which is related to the vibration mods of Fe–O bonds in the γ-Fe_2O_3 crystalline lattice.[45] The characteristic bands that appeared at 1617 and 3406 cm^{-1} are in turn certified to the bending and stretching vibrations of the surface hydroxyl groups and adsorbed water molecules.[49] As can be seen in the FT-IR spectrum of g-C_3N_4/γ-Fe_2O_3/TiO_2 (Figure 1c), the broad characteristic stretching vibration band of Ti–O at 498–769, which overlapped with the stretching vibrations of Fe–O bonds, is obvious. Moreover, the major characteristic bands of g-C_3N_4 could be easily detected in the g-C_3N_4/γ-Fe_2O_3/TiO_2 spectrum.

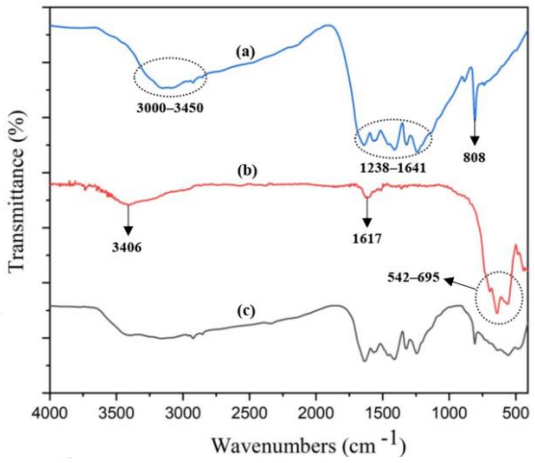

Figure 1. FT-IR spectrum of (a) g-C_3N_4, (b) γ-Fe_2O_3 and (c) g-C_3N_4/γ-Fe_2O_3/TiO_2.

XPS was performed to investigate the electronic features and elemental composition of g-C_3N_4/γ-Fe_2O_3/TiO_2 (Figure 2). As depicted in Figure 2a, the presence of the distinct characteristic peaks corresponding to C, N, O, Ti and Fe elements is confirmed in the XPS elemental survey of the catalyst. Figure 2b shows the high-resolution XPS spectra of C 1s in g-C_3N_4/γ-Fe_2O_3/TiO_2, which is deconvoluted into four main peaks. The peak observed at 284.6 eV could be assigned to the adventitious C-C bonds.[50] The signal observed at 285.9 eV is associated with the N-C_{sp2} bonds.[51] Two other peaks at 288.3 and 289.5 eV are emanated from the sp^2-hybridized C atoms bonded to N in an aromatic ring [N=C–$(N)_2$], and sp^2-hybridized C atoms in the aromatic rings bonded to the primary and secondary amines [N=C(N)–NH_2, N=C(N)–NH], respectively.[16] The high-resolution spectra of N 1s shown two indicative peaks centered at 398.8 and 400.5 eV, respectively (Figure 2c). The former is ascribed to the C-N=C and N-$(C)_3$ bonds, while the latter is associated with the C-N-H bonds.[26,52,53] As shown in Figure 2d, the high-resolution XPS spectra of O 1s of the catalyst exhibits two peaks at 529.7 eV (due to the TiO_2 or γ-Fe_2O_3 lattice oxygen atoms) and 531.2 eV (due to the OH groups or H_2O molecules absorbed on the catalyst surface).[2,26,50] In the Ti 2p spectrum of the catalyst (Figure 2e), two strong peaks with binding energies of about 458.4 and 464.2 eV, which are respectively relating to Ti $2p_{3/2}$ and Ti $2p_{1/2}$, could be assigned to Ti^{4+} in the TiO_2 lattice.[2,50] The high-resolution XPS spectra of Fe 2p (Figure 2f) illustrate four dominant peaks including Fe $2p_{3/2}$ at 710.3 and 712.4 eV, along with Fe $2p_{1/2}$ at 724.0 and 725.5 eV, which evidence the existence of Fe^{3+}.[54-57] The fitted Fe $2p_{3/2}$ peak at 710.3 eV, can be allocated to Fe^{3+} state in the Ti–O–Fe bond.[53] The absence of the Fe $2p_{3/2}$ peak at 709.3 eV suggests that no Fe^{2+} exists in the synthesized catalyst.[54]

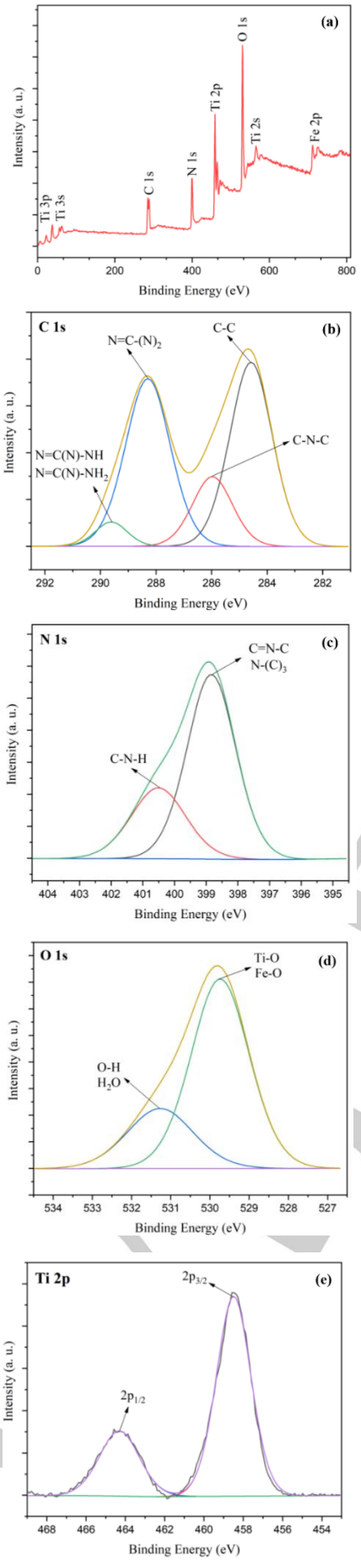

Figure 2. (a) XPS elemental survey spectrum, and high-resolution XPS spectra of (b) C 1s, (c) N 1s, (d) O 1s, (e) Ti 2p and (f) Fe 2p of g-C_3N_4/γ-Fe_2O_3/TiO_2.

XRD analysis was carried out to understand the structural features of the fabricated photocatalyst (Figure 3). Figure 3a presents the XRD pattern of γ-Fe_2O_3, which reveals a series of characteristic peaks appeared at 30.3°, 35.8°, 43.4°, 53,9°, 57.4° and 63° (2θ) that are associated with (2 2 0), (3 1 1), (4 0 0), (4 2 2), (5 1 1) and (4 4 0) planes of the cubic structure of maghemite (JCPDS card No. 04–0755).[40] As can be perceived from the XRD pattern of g-C_3N_4/γ-Fe_2O_3/TiO_2 (Figure 3b), the characteristic peaks relating to γ-Fe_2O_3 can be easily observed. Also, two indicative diffraction peaks at 27.4° and 13.1° (2θ) can be attributed to the (0 0 2) and (1 0 0) crystallographic faces of g-C_3N_4 in the photocatalyst.[33,58] The appearance of the characteristic peaks at around 25.3°, 37.8°, 48.2°, 54.2°, 55.3°, 62.5°, and 70.4° (2θ) corresponding to the (1 0 1), (0 0 4), (2 0 0), (1 0 5), (2 1 1), (2 0 4) and (2 2 0) plane diffractions, confirms the anatase phase formation of TiO_2 (JCPDS card No. 21-1272)[50] in the g-C_3N_4/γ-Fe_2O_3/TiO_2.

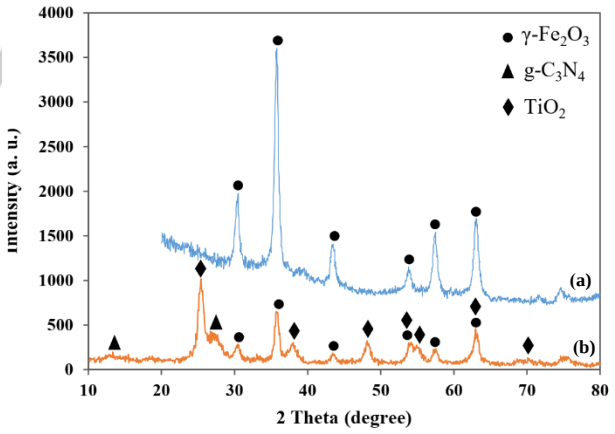

Figure 3. XRD patterns of (a) γ-Fe_2O_3 and (b) g-C_3N_4/γ-Fe_2O_3/TiO_2.

The magnetic features of γ-Fe_2O_3 and g-C_3N_4/γ-Fe_2O_3/TiO_2 were examined by VSM analysis at room temperature (Figure 4). As it could be perceived from the resulting magnetization curves, the saturation magnetization amounts of γ-Fe_2O_3 and g-C_3N_4/γ-Fe_2O_3/TiO_2 are 66.50 and 25.50 emu.g^{-1}, respectively. No detected hysteresis loop in the magnetization curves of both γ-Fe_2O_3 and g-C_3N_4/γ-Fe_2O_3/TiO_2 points out to their superparamagnetic feature.

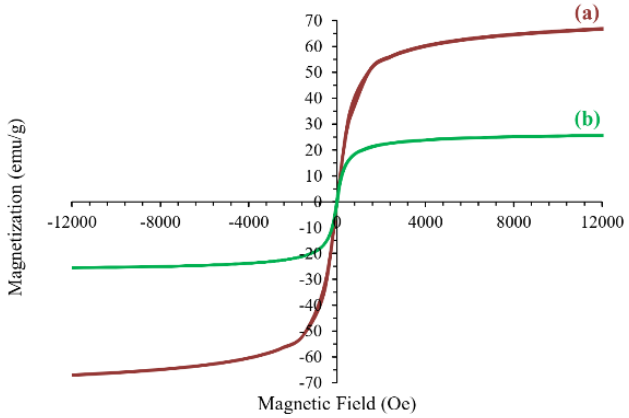

Figure 4. Magnetization curves of (a) γ-Fe_2O_3 and (b) g-C_3N_4/γ-Fe_2O_3/TiO_2.

The optical absorbance characteristics of the prepared nanocomposite were evaluated by UV-vis DRS. As it is obvious in Figure 5, the g-C_3N_4/γ-Fe_2O_3/TiO_2 revealed a supreme absorption in the visible-light area. Furthermore, according to the Tauc plot of $(\alpha h\nu)^2$ *vs.* hυ (Figure 6), the value of the band gap energy for g-C_3N_4/γ-Fe_2O_3/TiO_2 was estimated to be 2.6 eV, which proved the high capability of the catalyst to enhance the photoinduced electron-holes separation and improves its visible-light photocatalytic performance.

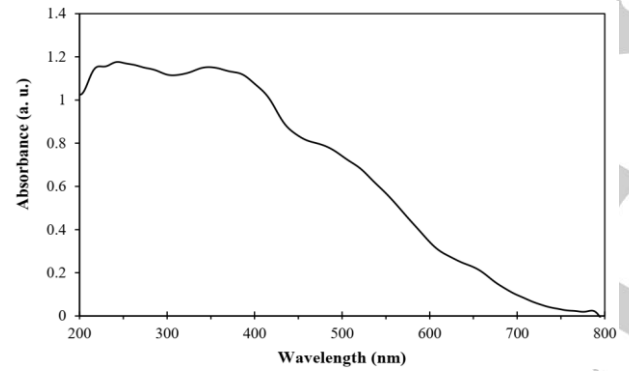

Figure 5. UV-vis DRS of g-C_3N_4/γ-Fe_2O_3/TiO_2.

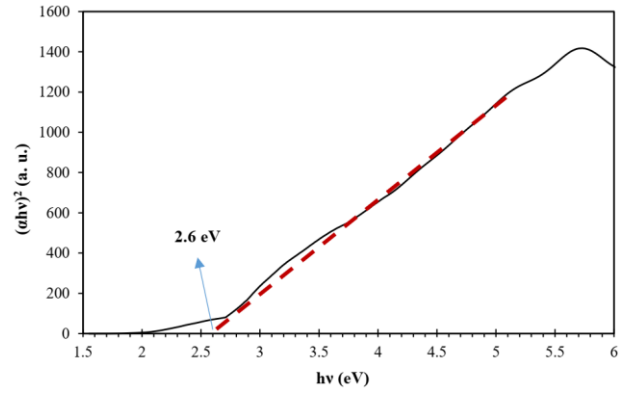

Figure 6. Tauc plot for band gap estimation of g-C_3N_4/γ-Fe_2O_3/TiO_2.

Moreover, the SEM and TEM images were evaluated to understand the morphological properties of the catalyst (Figure 7). As it is evident in Figure 7, the g-C_3N_4 sheets accompanied with the spherical γ-Fe_2O_3 and TiO_2 nanoparticles can be seen. As it is obvious in the TEM images, the mean sizes of the γ-Fe_2O_3 and TiO_2 particles were measured to be around 15-18 nm. Interestingly, the observed lattice fringe of about 0.35 nm, could be attributed to the (1 0 1) planes in the anatase phase of TiO_2[50] (Figure 7e).

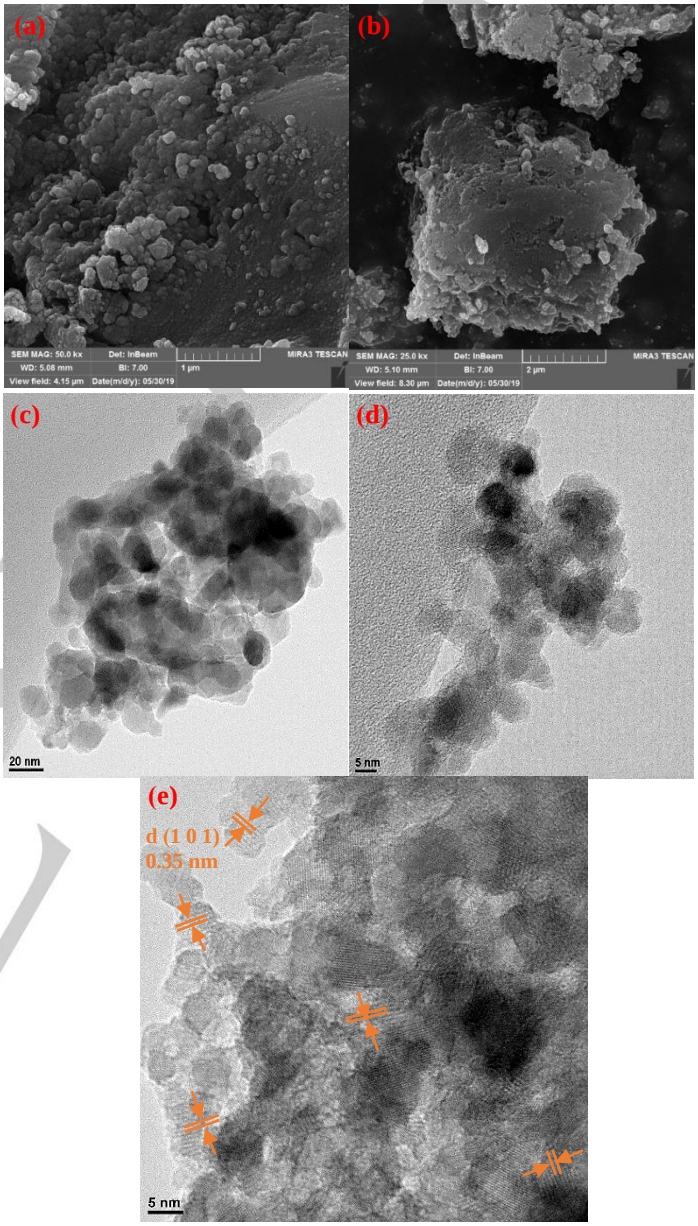

Figure 7. (a, b) SEM and (c-e) TEM images of g-C_3N_4/γ-Fe_2O_3/TiO_2.

The N_2 adsorption–desorption isotherm and the BJH pore size distribution plot of the photocatalyst are shown in Figure 8. Based on the results, the BET surface area, pore volume and mean pore diameter of the photocatalyst were 66.33 $m^2\ g^{-1}$, 0.14 $cm^3\ g^{-1}$ and 8.66 nm, respectively. In addition, the BJH calculations demonstrated a uniform pore size distribution with a high-intensity peak (Figure 8b).

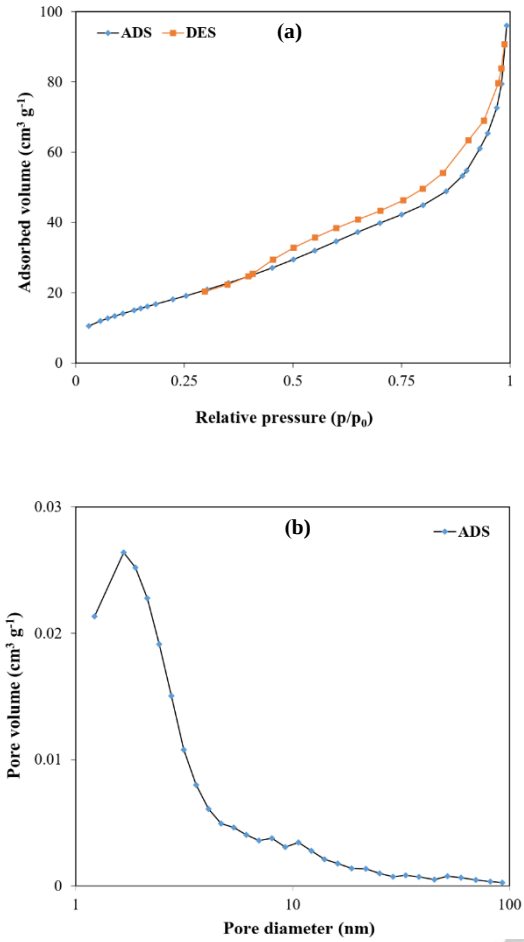

Figure 8. N_2 adsorption-desorption isotherm (a) and BJH pore size distribution plot (b) of g-C_3N_4/γ-Fe_2O_3/TiO_2.

EDS analysis of g-C_3N_4/γ-Fe_2O_3/TiO_2 disclosed the presence of C, O, N, Fe and Ti elements through their corresponding signal illustration, which further corroborated the successful fabrication of the nanocomposite (Figure 9a). Moreover, to explore the elemental composition uniformity of g-C_3N_4/γ-Fe_2O_3/TiO_2, elemental mapping analysis was conducted (Figure 9b-g). As it is evident, the simultaneous existence of C, O, N, Fe and Ti elements with homogeneous distribution on the entire surface of the catalyst was well proved.

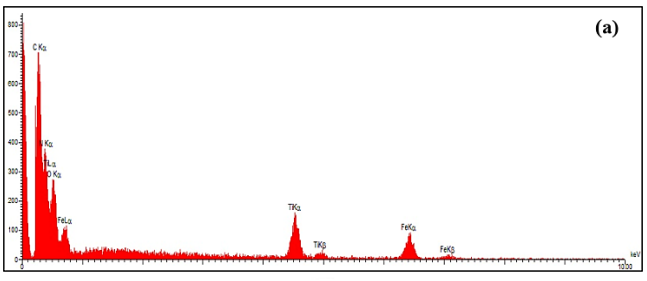

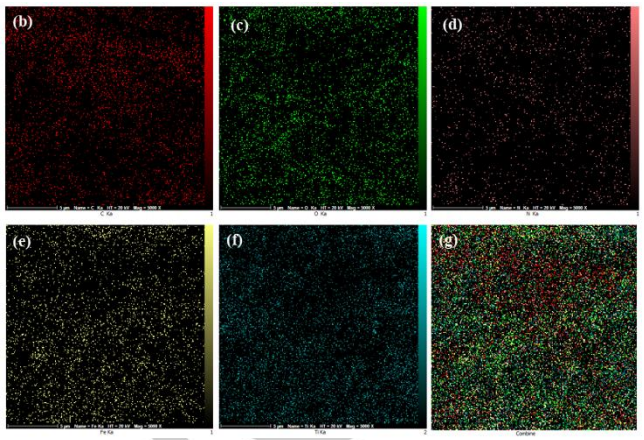

Figure 9. (a) EDS analysis and elemental mapping images of (b) carbon (red), (c) oxygen (green), (d) nitrogen (pink), (e) iron (yellow), (f) titanium (cyan) and (g) the overlapping of C, O, N, Fe and Ti elements in g-C_3N_4/γ-Fe_2O_3/TiO_2.

Designing the experiment and statistical investigations

In this study, for the process modeling, investigation of the influence of operational factors on the CEF photocatalytic degradation, and determining the actual optimal conditions, the CCD based on RSM was applied under the area of the design expert software (version 10.0). The five critical parameters affecting the degradation process including the CEF amount (mg/L, A), g-C_3N_4/γ-Fe_2O_3/TiO_2 concentration (g/L, B), pH (C), visible-light intensity (W/m^2, D) and contact time (min, E) were selected as the operational independent parameters. These factors were chosen according to the preliminary experiments. The efficiency of the CEF photocatalytic degradation process was examined as the dependent factor (response, R). The experimental ranges and the levels of the independent parameters are demonstrated in Table 1. The present designation indicates 32 individual experimental runs in two blocks, based on ½ fraction CCD experiments (Table 2).

It is worth noting that the antibiotic durability might be affected by changing the pH of the solution. To consider this issue, the CEF stability was evaluated at different pH amounts. As it is evident in the diagram of CEF absorbance *vs.* pH values (Figure 10), CEF is very stable up to pH of about 10.5 and then, the CEF absorbance begins to decrease. This observation is related to the hydrolysis of the CEF molecules due to the instability of the β-lactam ring at high pH amounts.[59,60] Therefore, CEF is completely stable in the selected pH range (0.5-10.5) of the experimental design[61] and so, all results regarding the CEF degradation are related to the photocatalytic behavior.

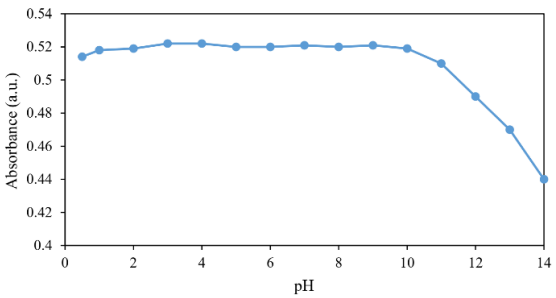

Figure 10. The effect of pH variations on the absorbance of the CEF.

Table 1. Experimental range and levels of the independent parameters used for the CEF degradation process in CCD.

Independent variables	Symbols	Range and levels				
		-α	-1	0	+1	+ α
CEF amount (mg/L)	A	10	15	20	25	30
Catalyst concentration (g/L)	B	0	0.02	0.04	0.06	0.08
pH	C	0.5	3	5.5	8	10.5
Light intensity (W/m^2)	D	3	6	9	12	15
Contac time (min)	E	30	60	90	120	150

Table 2. The obtained experimental values of the response in CCD.

Run	A	B	C	D	E	R (%)
1	15	0.06	8	12	60	41
2	20	0.04	10.5	9	90	4
3	20	0.04	5.5	9	30	60
4	10	0.04	5.5	9	90	84
5	15	0.02	8	6	60	34
6	15	0.02	8	12	120	44
7	15	0.06	3	6	60	33
8	25	0.02	8	6	120	15
9	20	0.04	5.5	9	150	58
10	20	0.04	5.5	3	90	65
11	20	0.04	5.5	9	90	98
12	15	0.02	3	6	120	27
13	30	0.04	5.5	9	90	69
14	20	0.04	5.5	9	90	97
15	15	0.02	3	12	60	40
16	15	0.06	8	6	120	24
17	20	0.08	5.5	9	90	8
18	20	0.04	5.5	9	90	97.8
19	20	0.04	0.5	9	90	13
20	25	0.06	8	12	120	31
21	25	0.02	3	6	60	20
22	20	0.04	5.5	15	90	97.5
23	20	0.04	5.5	9	90	98.3
24	25	0.06	8	6	60	18
25	15	0.06	3	12	120	50
26	25	0.06	3	6	120	31
27	20	0	5.5	9	90	0
28	20	0.04	5.5	9	90	98.7
29	25	0.02	8	12	60	31
30	20	0.04	5.5	9	90	98.5
31	25	0.02	3	12	120	37
32	25	0.06	3	12	60	45

Method modeling

Analysis of variance (ANOVA) was performed to evaluate the statistical significance level and adequacy of the model.[62] In the ANOVA analysis, when the data related to the p-value was determined to be lower than 0.05, the fitted model would be proper for predicting the photocatalytic degradation process at a confidence level of 95%.[63,64] Furthermore, the lack-of fit (LOF) of the model should be insignificant to well represent the high performance of the model for providing reasonable data.[63,64] Accordingly, the designated data to the p-value and LOF amount in Table 3, clearly revealed that the designed model is extremely significant and proper to use for the experimental range evaluated.

Using this procedure, an empirical quadratic polynomial equation was achieved to model the interaction of the five independent parameters (A-E) on the efficiency of the photocatalytic degradation of CEF (R), as follows:

$$R = +98.09 - 3.96*A + 1.71*B - 2.62*C + 7.58*D - 0.29*E + 1.19*AB - 1.94*AC - 2.81*BC - 1.06*CE + 0.81*DE - 5.43*A^2 - 23.56*B^2 - 22.43*C^2 - 4.24*D^2 - 9.81*E^2$$

in which, parameters with a positive sign (+) and a negative sign (–) have a positive and negative influence on the CEF photocatalytic degradation process, respectively.
The high value of R^2 (0.9996) and the adjusted R^2 (0.9992), and their closeness to 1.0 shows a very reasonable agreement between the observed results and the predicted ones.[64]
To obtain further insight into the accuracy of the model in the CEF degradation process, the predicted values obtained from the respective model versus the measured experimental data (actual values) are depicted in Figure 11a. As it is apparent, the predicted data are entirely close to the experimental ones, which successfully confirmed that the actual values are well agreed with the predicted results, in accordance with the proposed polynomial equation.[63] In addition, the respective normal probability plot of residuals for the response (Figure 11b) clearly illustrates that the resulting data points are constantly exposed on a straight-line basis. These findings revealed that there is no clear dispersal in the obtained data and the error variance is homogeneous.[65] Besides, the good fit of the model was analyzed by constructing the externally studentized residual values versus the experimental runs and indicated that all data points were placed within the limits[66] (Figure 11c).

Table 3. The ANOVA obtained data for the response surface quadratic model of the CEF degradation process.

Source	Sum of Squares	DF	Mean Square	F-Value	p-value	
Model	32112.83	15	2140.86	2503.11	< 0.0001	significant
A	376.04	1	376.04	439.67	< 0.0001	
B	70.04	1	70.04	81.89	< 0.0001	
C	165.38	1	165.38	193.36	< 0.0001	
D	1380.17	1	1380.17	1613.70	< 0.0001	
E	2.04	1	2.04	2.39	0.1419	
AB	22.56	1	22.56	26.38	< 0.0001	
AC	60.06	1	60.06	70.23	< 0.0001	
BC	126.56	1	126.56	147.98	< 0.0001	

CE	18.06	1	18.06	21.12	0.0003	
DE	10.56	1	10.56	12.35	0.0029	
A^2	865.11	1	865.11	1011.49	< 0.0001	
B^2	16276.19	1	16276.19	19030.26	< 0.0001	
C^2	14758.64	1	14758.64	17255.93	< 0.0001	
D^2	528.13	1	528.13	617.50	< 0.0001	
E^2	2820.44	1	2820.44	3297.68	< 0.0001	
Residual	13.68	16	0.86			
Lack of Fit	11.83	11	1.08	2.90	0.1250	not significant
Pure Error	1.86	5	0.37			
Cor. Total	32126.52	31				

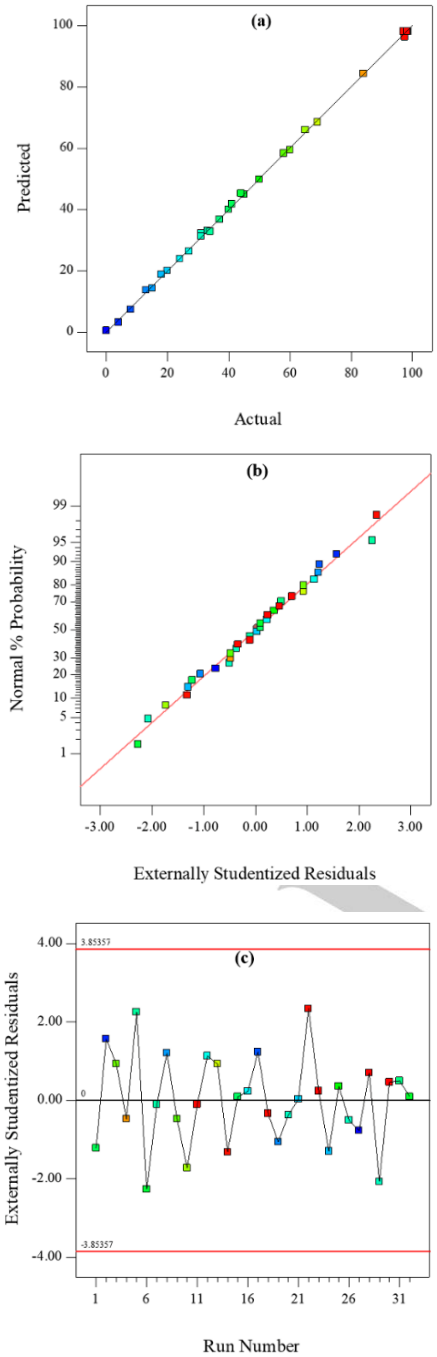

Figure 11. (a) Predicted values versus actual data, (b) normal probability plot of the residuals and (c) residual values versus the experimental runs diagnostic plots for the CCD model adequacy.

Investigation of the interactive effects of studied factors

Three-dimensional (3D) response surface and two-dimensional (2D) contour plots were conducted to discover the effects of independent parameters on the removal behavior of the system with regard to all significant interactions in the RSM-CCD.[67] In fact, the interactive effect of each two parameters and the relationship between them could be well perceived by exploring the related contour plots. To understand the effect of each pair of parameters on the response, 3D response surface plots were employed.

Figure 12 shows the contour and the 3D plots to probe the effects of independent significant factors on the CEF degradation efficiency. In each experiment, the interaction of two separate factors and their simultaneous effect on the response were evaluated by keeping the other factors at the middle values. As it is clear, when the catalyst concentration was enhanced to 0.04 g/L, the amount of CEF degradation was also increased. However, when the catalyst concentration increased further, the degradation process rate was diminished (Figures 12a and 12b). Likewise, the effect of CEF amount on the photocatalytic degradation percentage showed that at lower concentrations (below 20 mg/L) more photocatalytic degradation efficiency would be achieved and as the CEF amount elevated, the efficiency diminished (Figures 12a and 12b). Both of these observations could be related to the fact that the light scattering was reduced owing to the turbidity, which leads to less photocatalytic degradation.[68] The effects of the contact time and visible-light intensity are also depicted in Figure 12c and 12d. As can be seen, the highest percentage of CEF degradation was attained under 9 W/m^2 light intensity in 90 min. In fact, by improving the irradiation intensity to a certain amount (9 W/m^2), the efficiency of the degradation process was improved, and then the degradation rate was dropped slightly owing to the consumption of the produced hydroxyl radicals by the CEF molecules in solution.[69] Moreover, increasing the contact time to 90 min, increased the CEF degradation, while with more time enhancement, no obvious improvement was detected in the progress of the degradation process due to the absence of enough active hydroxyl radicals in the solution. As can be readily perceived from Figure 12e-j, the optimum pH value for CEF degradation is about 5.5.

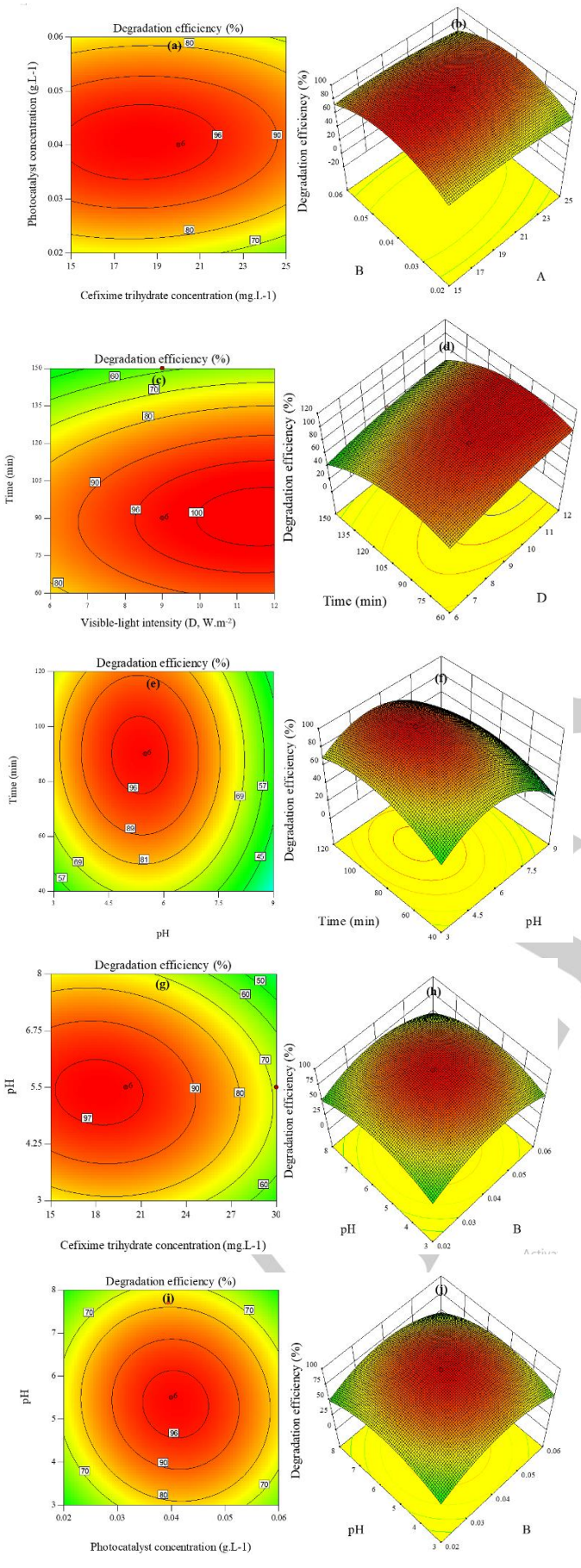

Figure 12. (a, c, e, g, i) The contour and (b, d, f, h, j) response surface plots for degradation efficiency of CEF (%).

Evaluation of the optimal conditions

Optimization of the influencing factors on the CEF degradation efficiency was conducted through the numerical optimization matrix based on the design expert software. Accordingly, the maximum degradation efficiency of 98.09% was predicted by the attained model for the CEF degradation at optimal conditions (CEF amount of 20 mg/L, catalyst concentration of 0.04 g/L, pH of 5.5, irradiation intensity of 9 W/m^2 and 90 min). To verify the predicted responses reliability at the optimized conditions, three experiments were performed at similar optimized conditions. The obtained results were accompanied by the average degradation percentage of 98.00% for CEF degradation, which is well agreed with the corresponding predicted data. The reliability of the proposed model was therefore confirmed by this rational agreement. In the following, control tests were done under the optimum conditions to more clarify the photocatalytic capability of the g-C_3N_4/γ-Fe_2O_3/TiO_2. For this purpose, the photolysis of CEF under the visible blue LED illumination in the absence of the catalyst, and the probability of the CEF adsorption on the catalyst surface at dark conditions were examined. As displayed in Figure 13, the photolysis experiment revealed no progress in the degradation process. Likewise, the adsorption capability of the photocatalyst for CEF under the dark condition was less than 5%. Moreover, when a similar experiment was carried out under the visible green LED irradiation, while all other conditions kept in the optimal set, the photocatalytic degradation behavior towards the CEF, was not promising. This is due to the fact that the green LED wavelength (530 nm) is higher than the blue LED one (475 nm). Indeed, as can be seen in Figure 6, the Tauc plot revealed that the band gap amount of the photocatalyst was about 2.6 eV, which is precisely in compliance with the absorption wavelength of the blue LED irradiation. Therefore, the best photocatalytic performance could certainly obtain in the presence of the blue LED illumination. The ability of the pure g-C_3N_4 for the photocatalytic degradation of the CEF was also probed and the degradation capability was calculated to be 63% under the optimal conditions. However, it is observable that by using g-C_3N_4/γ-Fe_2O_3/TiO_2 under the optimum conditions, the best efficiency of the CEF degradation achieved within 90 minutes. This enhancement in the degradation rate can be ascribed to the synergistic optical effects between g-C_3N_4, γ-Fe_2O_3, and TiO_2, which increased the charge carriers' production and well slowed down the speed of the electron-hole pairs' recombination (Figure 13).

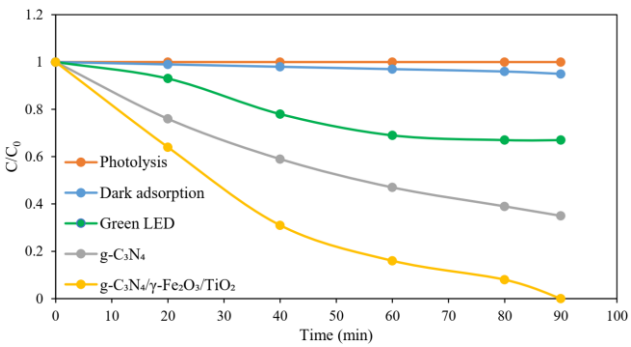

Figure 13. Photocatalytic degradation of CEF under the visible-light irradiation in optimum conditions.

TOC analysis

Total organic carbon (TOC) analysis was accomplished to quantitatively monitor the mineralization process of the CEF under the optimal conditions. The percentage of TOC degradation can be determined by using the following equation:

$$\% \text{ TOC degradation} = \frac{(TOC)0-(TOC)t}{(TOC)0} \times 100$$

where $(TOC)_0$ = Initial TOC of the CEF solution and $(TOC)_t$ = TOC of the CEF solution at specific reaction time during treatment with nanocomposite.

As it is depicted in Figure 14, the capability of the CEF degradation measured from the TOC analysis revealed a trend similar to the data obtained by the UV-vis study. In fact, the molecules of CEF were almost quite photodegraded to very small segments. These results more endorsed the efficiency of the presented nanocomposite for the mineralization of CEF.

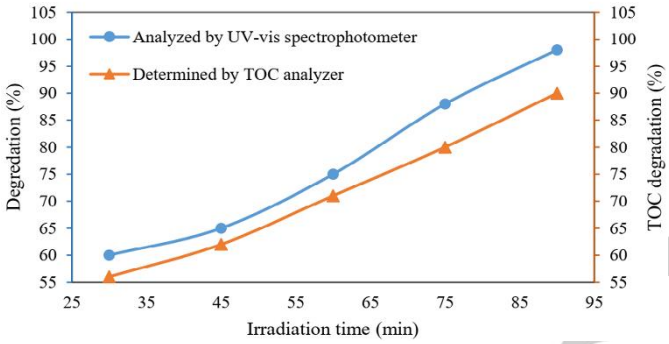

Figure 14. Degradation rate of CEF using g-C_3N_4/γ-Fe_2O_3/TiO_2 photocatalyst obtained from the absorbance measurements (blue circle) and TOC analysis (red triangle) versus the irradiation time.

Kinetic study

Evaluation of the reaction rate kinetics is a fundamental aspect in the catalytic wastewater purification processes. The Langmuir–Hinshelwood (L-H) kinetic model is applied to investigate the photocatalytic degradation kinetics of many organic compounds such as antibiotics.[70] In fact, a beneficial photocatalytic degradation route follows the pseudo first-order kinetics according to the L-H model, which can be defined as the bellow equation:

$$\ln\left(\frac{Co}{Ct}\right) = -kt$$

where, k is defined as the pseudo first-order rate constant, C_0 is the initial contaminant concentration and C_t is the contaminant concentration at time t.
To probe the photocatalytic degradation kinetics of CEF in the presence of the present catalyst, some typical tests were performed under the optimum conditions (catalyst concentration: 0.04 g/L, pH= 5.5 and irradiation intensity: 9 W/m^2) for different CEF amounts within the range of 20-90 min. Results revealed the existence of a linear relation between ln (C_0/C_t) and t, verified that the photocatalytic degradation process followed a real pseudo first-order kinetic (Figure 15).

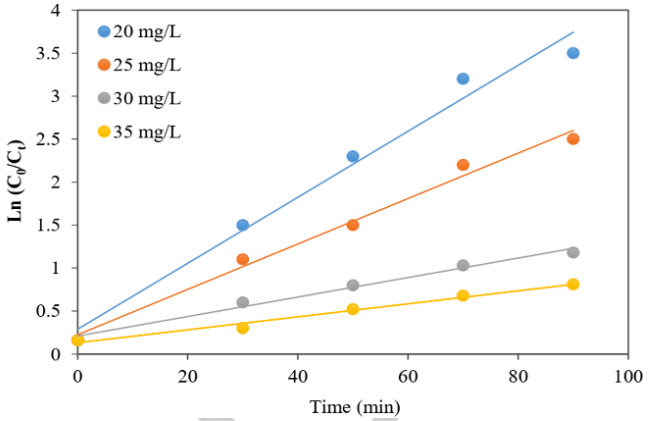

Figure 15. Plots of the L-H kinetic model ln (C_0/C_t) *vs*. contact time, for CEF photocatalytic degradation at different concentrations (pH=5.5, catalyst value = 0.04 g/L, and irradiation intensity = 9 W/m^2).

Also, the R^2 values were obtained close to 1 for all different concentrations of CEF, which further approved the suitability of the model (Table 4). As can be seen in Table 4, when the CEF amount was increased, the reaction rate constants diminished. This might be ascribed to the enhancement of the transition products at higher CEF amounts, which led to reduce the potent hydroxyl radicals in the solution and also the degradation rate constants.[71]

Table 4. Kinetic parameters for CEF photocatalytic degradation reactions at different concentrations.

Entry	CEF amount (mg/L)	Equation	K (min^{-1})	R^2
1	20	y = 0.0384x + 0.2895	38.4 × 10^{-3}	0.9811
2	25	y = 0.0264x + 0.2239	26.4 × 10^{-3}	0.9885
3	30	y = 0.0113x + 0.2097	11.4 × 10^{-3}	0.9862
4	35	y = 0.0076x + 0.1307	7.6 × 10^{-3}	0.9835

Reusability of g-C_3N_4/γ-Fe_2O_3/TiO_2 nanocomposite in the CEF photocatalytic degradation process

Recyclability of the photocatalysts is a crucial parameter to reduce the operating costs in practical applications. In this regard, to evaluate the reusability and durability of g-C_3N_4/γ-Fe_2O_3/TiO_2, seven repeated cycles of the CEF photocatalytic degradation were done under the optimal conditions. After each run, the photocatalyst was isolated from the aqueous solution employing a magnetic field, washed three times with distilled water, oven-dried at 70 °C within 2 h and reused in the next run. Based on the results displayed in Figure 16, no substantial change was witnessed in g-C_3N_4/γ-Fe_2O_3/TiO_2 photocatalytic reactivity even after seven runs of recycling. The slight reduction in the degradation rate of CEF after seven consecutive runs might be due to the small loss of the photocatalyst throughout the recycling procedure. Moreover, comparing the FT-IR spectrum of seven times reused catalyst (Figure 17) with the fresh one (Figure 1c) indicated that the structure and morphology of the photocatalyst were not changed after seven consecutive runs. These findings imply the high stability and reusability of the presented nanocomposite.

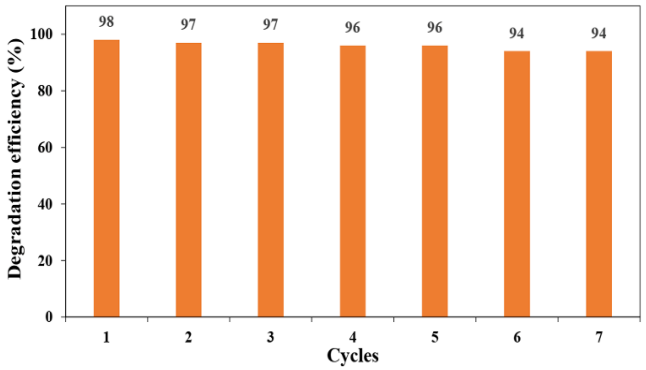

Figure 16. Results of the recycling studies of nanocomposite in the photocatalytic degradation of CEF.

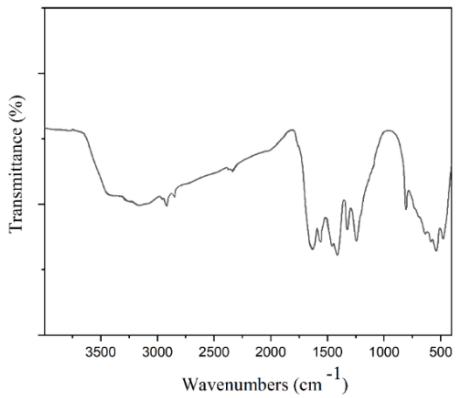

Figure 17. FT-IR spectrum of g-C_3N_4/γ-Fe_2O_3/TiO_2 after seven times reused.

Comparative study

To clarify the merits of the suggested method over the previously reported procedures towards the CEF photocatalytic degradation, the effectiveness of the current catalytic system was compared with the hitherto reported catalytic systems in the literature (Table 5). It can be evidently observed that the present photocatalytic system is premier to the reported procedures. The superior photocatalytic reactivity of the current catalyst might be related to synergistic optical effects between g-C_3N_4, γ-Fe_2O_3, and TiO_2, which increased the charge carriers' production and well slowed down the speed of the electron-hole pairs' recombination. Moreover, the present photocatalyst was simply isolated by an external magnetic field.

Proposed photocatalytic mechanism for the CEF photocatalytic degradation by g-C_3N_4/γ-Fe_2O_3/TiO_2

To detect the main oxidative species in the photocatalytic degradation process of CEF, the trapping experiments were performed using radical and hole scavengers. To do this, the photocatalytic degradation of CEF in the optimal conditions was conducted in the presence of *tert*-butyl alcohol (*t*-BuOH), *p*-benzoquinone (BQ), and ammonium oxalate (AO) as the hydroxyl radical, superoxide radical, and hole scavengers, respectively (Figure 18). As can be seen, the photocatalytic degradation efficiency of CEF using g-C_3N_4/γ-Fe_2O_3/TiO_2 photocatalyst was about 98% without any scavenger after visible-light irradiation for 90 min. By the addition of *t*-BuOH (1 mM) into the reaction solution, the photocatalytic degradation efficiency of CEF was moderately affected. However, the photocatalytic degradation efficiency of CEF dropped substantially by adding BQ (1 mM) or AO (1 mM) to the reaction medium. These observations proposed that the superoxide radicals and holes are the main active species in the presented photocatalytic degradation system.

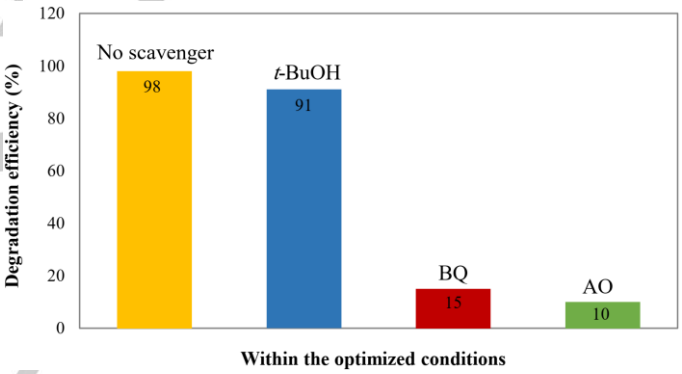

Figure 18. Effects of radical and hole scavengers on the photocatalytic degradation efficiency of CEF in the presence of the g-C_3N_4/γ-Fe_2O_3/TiO_2 photocatalyst, within the optimized conditions.

Table 5. Comparison of the photocatalytic performance of g-C_3N_4/γ-Fe_2O_3/TiO_2 with the reported photocatalytic systems for CEF degradation.

Entry	Photocatalyst	Catalyst amount ($g.L^{-1}$)	CEF amount ($mg.L^{-1}$)	Light source	Oxidant	pH	Time (min)	Degradation efficiency (%)	Ref.
1	NiO/NCP[a]	0.25	5	Hg-lamp (UV-A), 75 W	air	5	180	70	[36]
2	Nano-crystalline ZnO	-	20	UV black lamp, 27 W/m^2	air	-	28	-	[39]
3	Nano α-Fe_2O_3/ZnO	0.41	10.11	UV-vis, 8 W	air	9	127	99.1	[38]
4	TiO_2/NHG[b]	0.05	25	sunlight	H_2O_2 (5mg/L)	-	90	92.3	[3]
5	g-C_3N_4/γ-Fe_2O_3/TiO_2	0.04	20	Visible blue-LED, 9 W/m^2	air	5.5	90	98.09	Present work

[a] NiO/nano-clinoptilolite. [b] TiO_2/nitrogen doped holey graphene hybrid

According to the above results, a plausible photocatalytic mechanism was proposed for the CEF photocatalytic degradation in the presence of g-C_3N_4/γ-Fe_2O_3/TiO_2 under visible-light irradiation (scheme 2). As it is clear, scheme 2 shows the electron-hole separation and charge transfer pathway at the g-C_3N_4/γ-Fe_2O_3/TiO_2 photocatalyst interfaces. Under the visible blue LED light irradiation, g-C_3N_4 and γ-Fe_2O_3 can be easily excited to generate electrons and holes. Then, the photogenerated electrons from the conduction bond (CB) of g-C_3N_4 can be simply transferred into the CB of γ-Fe_2O_3 and simultaneously the existing electrons immigrated from the CB of γ-Fe_2O_3 to the CB of TiO_2. On the other hand, the photogenerated holes in the valence bond

(VB) of γ-Fe_2O_3 can easily be injected into the VB of g-C_3N_4. These appropriate charge carriers' transformations along the heterojunction interfaces of the photocatalyst led to efficient separation of photogenerated electrons/holes and a prolonged lifetime of the excited electrons/holes, as well. Electrons in the CB of TiO_2 will further adsorb the oxygen molecules from the solution to make the superoxide radical ions, which are potent oxidative species for the degradation of CEF. Meanwhile, the accumulated holes presented in the VB of g-C_3N_4 would react directly with the CEF molecules.

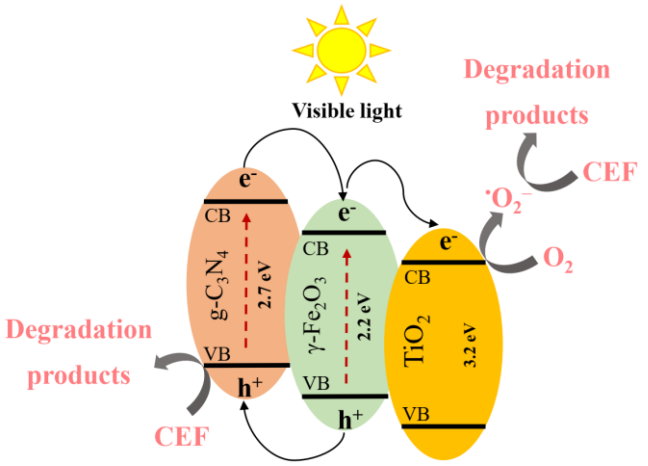

Scheme 2. Proposed photocatalytic mechanism for CEF photocatalytic degradation using g-C_3N_4/γ-Fe_2O_3/TiO_2 nanocomposites under visible blue LED light irradiation.

Conclusions

g-C_3N_4/γ-Fe_2O_3/TiO_2 was successfully prepared and fully characterized by FT-IR, XPS, XRD, VSM, DRS, SEM, TEM, BET, EDS, and elemental mapping techniques. The capability of the synthesized g-C_3N_4/γ-Fe_2O_3/TiO_2 as an effective magnetically separable and visible-light-driven photocatalyst (band gap energy = 2.6 eV) was satisfactorily evaluated for the degradation process of CEF. The optimization of the operational parameters in the photocatalytic degradation process of CEF was studied by the mathematical and statistical approaches using CCD based on RSM. Results indicated that the photocatalytic degradation efficiency of the CEF is equal to 98.09% under optimal conditions (CEF amount = 20 mg/L, g-C_3N_4/γ-Fe_2O_3/TiO_2 concentration = 0.04 g/L, pH = 5.5, irradiation intensity = 9 W/m^2 and contact time = 90 min). Based on the total organic carbon (TOC) analysis, the CEF molecules were almost quite photodegraded to very small segments (percentage of TOC degradation = 90%). Interestingly, the superlative photocatalytic performance of the catalyst could be ascribed to the synergistic optical effects between g-C_3N_4, γ-Fe_2O_3, and TiO_2, which can increase the charge carriers production and also overcome the fast recombination rate of the photoinduced electron-hole pairs. Moreover, the photocatalyst was simply separated by the aid of an external magnet and recycled for seven sequential runs with no substantial reduction in its reactivity. In this study, the obtained experimental values well follow the pseudo first-order kinetics according to the L-H model. Using a capable visible-light harvesting photocatalyst, employing a superparamagnetic photocatalyst with convenient isolation ability, almost complete mineralization of the CEF in the presence of a very low amount of the photocatalyst under an eco-benign and innocuous visible-light source by air as the oxidant, could be considered as the major highlights of the presented protocol, which support it well towards the green chemistry.

Supporting Information Summary

Acknowledgements

Financial support of this project by the University of Birjand Research Council and the XPS facilities of the University of Alicante is appreciated. The guidance of Dr. Rouhollah Khani for using design expert software and also Prof. Mehrorang Ghaedi for some advices are acknowledged.

Keywords: Carbon nitride • Cefixime trihydrate • Photocatalysis • Visible-light • Wastewater treatment • Heterogeneous catalysis

[1] B. Song, G. Zeng, J. Gong, J. Liang, P. Xu, Z. Liu, Y. Zhang, C. Zhang, M. Cheng, Y. Liu, S. Ye, *Environ. Int.* **2017**, *105*, 43-55.
[2] Z. Yang, J. Yan, J. Lian, H. Xu, X. She, H. Li, *ChemistrySelect* **2016**, *1*, 5679-5685.
[3] C. Shaniba, M. Akbar, K. Ramseena, P. Raveendran, B. N. Narayanan, R. M. Ramakrishnan, *J. Environ. Chem. Eng*. **2020**, *8*, 102204.
[4] J. Blackbeard, J. Lloyd, M. Magyar, J. Mieog, K. G. Linden, Y. Lester, *Environ. Sci. Water Res. Technol.* **2016**, *2*, 213-222.
[5] E. S. Elmolla, M. Chaudhuri, *Desalination* **2010**, *256*, 43-47.
[6] Z. Derakhshan, M. Mokhtari, F. Babaie, R. M. Ahmadi, M. H. Ehrampoosh, M. Faramarzian, *J. Environ. Health Sustain. Dev*. **2016**, *1*, 43-62.
[7] K. Slipko, D. Reif, M. Wögerbauer, P. Hufnagl, J. Krampe, N. Kreuzinger, *Water Res*. **2019**, *164*, 114916.
[8] T. Saitoh, K. Shibata, K. Fujimori, Y. Ohtani, *Sep. Purif. Technol*. **2017**, *187*, 76-83.
[9] L. Ji, W. Chen, L. Duan, D. Zhu, *Environ. Sci. Technol*. **2009**, *43*, 2322-2327.
[10] Y. Li, L. Liu, F. Yang, *J. Membr. Sci*. **2017**, *525*, 202-209.
[11] C. Hachem, F. Bocquillon, O. Zahraa, M. Bouchy, *Dyes pigments* **2001**, *49*, 117-125.
[12] X. H. Qi, Y. Y. Zhuang, Y. C. Yuan, W. X. Gu, *J. Hazard. Mater*. **2002**, *90*, 51-62.
[13] M. Umar, H. A. Aziz in *Organic pollutants-monitoring, risk and treatment*, *vol. 8* (Ed.: M. N. Rashed), BoD–Books on Demand, Bahman, IntechOpen, **2013**, pp. 196-197, DOI: 10.5772/53699.
[14] C. Chen, W. Ma, J. Zhao, *Chem. Soc. Rev*. **2010**, *39*, 4206-4219.
[15] G. H. Safari, M. Hoseini, M. Seyedsalehi, H. Kamani, J. Jaafari, A. H. Mahvi, *Int. J. Environ. Sci. Technol*. **2015**, *12*, 603-616.
[16] Z. Zeng, K. Li, K. Wei, Y. Dai, L. Yan, H. Guo, X. Luo, *Chin. J. Catal*. **2017**, *38*, 498-507.
[17] Z. Li, F. Raziq, C. Liu, L. Bai, L. Jing, *Curr. Opin. Green Sustain. Chem*. **2017**, *6*, 57-62.
[18] M. Mousavi, A. Habibi-Yangjeh, S. R. Pouran, *J. Mater. Sci. Mater. El*. **2018**, *29*, 1719-1747.
[19] S. Patnaik, S. Martha, S. Acharya, K. M. Parida, *Inorg. Chem. Front*. **2016**, *3*, 336-347.
[20] Z. Tong, D. Yang, Z. Li, Y. Nan, F. Ding, Y. Shen, Z. Jiang, *ACS nano* **2017**, *11*, 1103-1112.
[21] F. Wang, Y. Wang, Y. Feng, Y. Zeng, Z. Xie, Q. Zhang, Y. Su, P. Chen, Y. Liu, K. Yao, W. Lv, *Appl. Catal. B-Environ*. **2018**, *221*, 510-520.
[22] Y. He, Y. Wang, L. Zhang, B. Teng, M. Fan, *Appl. Catal. B-Environ*. **2015**, *168*, 1-8.
[23] Y. He, L. Zhang, M. Fan, X. Wang, M. L. Walbridge, Q. Nong, Y. Wu, L. Zhao, *Sol. Energy Mater. Sol. Cells* **2015**, *137*, 175-184.
[24] Y. Liu, Y. X. Yu, W. D. Zhang, *Int. J. Hydrog. Energy* **2014**, *39*, 9105-9113.
[25] J. Theerthagiri, R. A. Senthil, A. Priya, J. Madhavan, R. J. V. Michael, M. Ashokkumar, *RSC Adv*. **2014**, *4*, 38222-38229.

[26] Z. Tong, D. Yang, T. Xiao, Y. Tian, Z. Jiang, *Chem. Eng. J.* **2015**, *260*, 117-125.
[27] S. Ye, L. G. Qiu, Y. P. Yuan, Y. J. Zhu, J. Xia, J. F. Zhu, *J. Mater. Chem. A* **2013**, *1*, 3008-3015.
[28] Y. Ding, L. Zhou, L. E. Mo, L. Jiang, L. Hu, Z. Li, S. Chen, S. Dai, *Adv. Funct. Mater*. **2015**, *25*, 5946-5953.
[29] B. Roose, S. Pathak, U. Steiner, *Chem. Soc. Rev*. **2015**, *44*, 8326-8349.
[30] G. Wang, H. Wang, Y. Ling, Y. Tang, X. Yang, R. C. Fitzmorris, C. Wang, J. Z. Zhang, Y. Li, *Nano lett*. **2011**, *11*, 3026-3033.
[31] A. Ibhadon, P. Fitzpatrick, *Catalysts* **2013**, *3*, 189-218.
[32] R. Daghrir, P. Drogui, D. Robert, *Ind. Eng. Chem. Res*. **2013**, *52*, 3581-3599.
[33] J. Li, Y. Liu, H. Li, C. Chen, *J. Photochem. Photobiol. A Chem*. **2016**, *317*, 151-160.
[34] X. Lu, Q. Wang, D. Cui, *J. Mater. Sci. Technol*. **2010**, *26*, 925-930.
[35] R. Jain, V. K. Gupta, N. Jadon, K. Radhapyari, *Anal. Biochem*. **2010**, *407*, 79-88.
[36] A. Pourtaheri, A. Nezamzadeh-Ejhieh, *Chem. Eng. Res. Des*. **2015**, *104*, 835-843.
[37] Z. Masoudyfar, S. Elhami, *Spectrochim. Acta A* **2019**, *211*, 234-238.
[38] N. M. Shooshtari, M. M. Ghazi, *Chem. Eng. J*. **2017**, *315*, 527-536.
[39] M. Visalakshi, G. S. Bai, V. Sinduri, G. Praveena, G. Ushasree, G. Swapna, *International Conference on Advanced Nanomaterials & Emerging Engineering Technologies* (pp. 409-411), Chennai, July, **2013**.
[40] S. Sobhani, R. Jahanshahi, *New J. Chem*. **2013**, *37*, 1009-1015.
[41] S. Sobhani, F. Khakzad, *Appl. Organomet. Chem*. **2017**, *31*, e3877.
[42] S. Sobhani, S. Asadi, M. Salimi, F. Zarifi, *J. Organomet. Chem*. **2016**, *822*, 154-164.
[43] S. Sobhani, Z. M. Falatooni, S. Asadi, M. Honarmand, *Catal. Lett.* **2016**, *146*, 255-268.
[44] S. Sobhani, A. Habibollahi, Z. Zeraatkar, *Org. Process Res. Dev*. **2019**, *23*, 1321-1332.
[45] S. Sobhani, Z. Vahidi, Z. Zeraatkar, S. Khodadadi, *RSC Adv*. **2015**, *5*, 36552-36559.
[46] S. Sobhani, Z. Zeraatkar, F. Zarifi, *New J. Chem*. **2015**, *39*, 7076-7085.
[47] A. Thomas, A. Fischer, F. Goettmann, M. Antonietti, J. O. Müller, R. Schlögl, J. M. Carlsson, *J. Mater. Chem.* **2008**, *18*, 4893-4908.
[48] V. N. Khabashesku, J. L. Zimmerman, J. L. Margrave, *Chem. Mater*. **2000**, *12*, 3264-3270.
[49] Y. Gao, Y. Masuda, Z. Peng, T. Yonezawa, K. Koumoto, *J. Mater. Chem*. **2003**, *13*, 608-613.
[50] X. N. Wei, H. L. Wang, *J. Alloys Compd*. **2018**, *763*, 844-853.
[51] A. Habibi-Yangjeh, M. Mousavi, K. Nakata, *J. Photochem. Photobiol. A Chem*. **2019**, *368*, 120-136.
[52] H. Ji, F. Chang, X. Hu, W. Qin, J. Shen, *Chem. Eng. J*. **2013**, *218*, 183-190.
[53] A. Mirzaei, Z. Chen, F. Haghighat, L. Yerushalmi, *Appl. Catal. B-Environ*. **2019**, *242*, 337-348.
[54] M. H. Pham, C. T. Dinh, G. T. Vuong, N. D. Ta, T. O. Do, *Phys. Chem. Chem. Phys*. **2014**, *16*, 5937-5941.
[55] S. Srivastava, S. Badrinarayanan, A. J. Mukhedkar, *Polyhedron* **1985**, *4*, 409-414.
[56] R. Suresh, K. Giribabu, R. Manigandan, A. Stephen, V. Narayanan, *RSC Adv*. **2014**, *4*, 17146-17155.
[57] B. J. Tan, K. J. Klabunde, P. M. Sherwood, *Chem. Mater*. **1990**, *2*, 186-191.
[58] S. Pany, K. M. Parida, *Phys. Chem. Chem. Phys*. **2015**, *17*, 8070-8077.
[59] M. Sheydaei, H. R. K. Shiadeh, B. Ayoubi-Feiz, R. Ezzati, *Chem. Eng. J.* **2018**, *353*, 138-146.
[60] E. S. Elmolla, M. Chaudhuri, *Desalination* **2010**, *252*, 46-52.
[61] R. Mostafaloo, M. H. Mahmoudian, M. Asadi-Ghalhari, *J. Photochem. Photobiol. A Chem*. **2019**, *382*, 111926.
[62] R. D. C. Soltani, S. Jorfi, M. Safari, M. S. Rajaei, *J. Environ. Manage*. **2016**, *179*, 47-57.
[63] R. Khani, S. Sobhani, M. H. Beyki, *J. Colloid. Interface Sci*. **2016**, *466*, 198-205.
[64] S. Mosleh, M. R. Rahimi, M. Ghaedi, A. Asfaram, H. Javadian, F. Sadeghfarm R. Jannesar, *Appl. Organomet. Chem*. **2018**, *32*, e4513.
[65] D. Pokhrel, T. Viraraghavan, *Water Air Soil Pollut*. **2006**, *173*, 195.
[66] R. Khani, S. Sobhani, T. Yari, *Microchem. J.* **2019**, *146*, 471-478.
[67] R. Khani, S. Sobhani, M. H. Beyki, S. Miri, *Ecotox. Environ. Safe*. **2018**, *150*, 54-61.
[68] S. Sohrabi, F. Akhlaghian, *Process Saf. Environ*. **2016**, *99*, 120-128.
[69] R. D. C. Soltani, A. Rezaee, A. R. Khataee, M. Safari, *J. Ind. Eng. Chem*. **2014**, *20*, 1861-1868.
[70] J. Alvarez-Ramirez, R. Femat, M. Meraz, C. Ibarra-Valdez, *J. Math. Chem*. **2016**, *54*, 375-392.
[71] N. Nasseh, L. Taghavi, B. Barikbin, M. A. Nasseri, *J. Clean. Prod*. **2018**, *179*, 42-54.

Entry for the Table of Contents

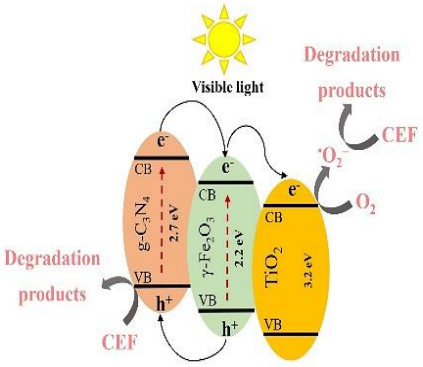

A magnetically separable g-C_3N_4/γ-Fe_2O_3/TiO_2 nanocomposite was synthesized as an intensely effectual visible-light-driven photocatalyst and fully characterized by different techniques. Surprisingly, the g-C_3N_4/γ-Fe_2O_3/TiO_2 presented a privileged photocatalytic performance for the CEF degradation under visible-light irradiation. In this study, CCD based on RSM was conducted for the optimization assessment of the operational factors.